Journal of Wind Engineering & Industrial Aerodynamics 220 (2022) 104837

Contents lists available at ScienceDirect

Journal of Wind Engineering & Industrial Aerodynamics

journal homepage: www.elsevier.com/locate/jweia

Experimental and numerical evaluation of the wind load on the 516 Arouca pedestrian suspension bridge

António Tadeu [a,d,*], F. Marques da Silva [b], Bahareh Ramezani [a], António Romero [c], Leopold Škerget [a], Filipe Bandeira [a]

[a] Itecons - Institute of Research and Technological Development in Construction, Energy, Environment and Sustainability, Rua Pedro Hispano, 3030-289, Coimbra, Portugal
[b] LNEC - National Laboratory for Civil Engineering, Structures Department, Av. do Brasil, 101, 1700-066, Lisboa, Portugal
[c] Escuela Técnica Superior de Ingeniería, Universidad de Sevilla, Camino de los Descubrimientos s/n, ES-41092, Sevilla, Spain
[d] ADAI-LAETA, University of Coimbra, Department of Civil Engineering, Faculty of Sciences and Technology. Pólo II, Rua Luís Reis Santos, 3030-788, Coimbra, Portugal

ARTICLE INFO

Keywords:
Computational fluid dynamics
World's longest pedestrian suspension bridge
Wind tunnel tests
Numerical results
Wind load

ABSTRACT

The present work analyses the wind load effects on the 516 Arouca bridge, the world's longest pedestrian suspension bridge in 2020. Computational fluid dynamics (CFD) was used to model a range of wind angles of attack between −8° and +8°. The simulations were performed by solving the steady-state Reynolds averaged Navier-Stokes (RANS) equations with the *k-ω* shear stress transport (SST) model. The fluid domain size was analysed by comparing the fluid flow behaviour for three different downstream sizes. It was shown that the downstream flow is not greatly affected by the bridge body due to the high opening surfaces of the bridge. Therefore, the most appropriate domain size considering the computation time was selected. The simulations were carried out for different bridge configurations to determine the influence of the upper guard of the tray deck and the suspended cables on the generated loads. The numerical results were validated by performing different wind tunnel tests using a reduced scale prototype. The predicted aerodynamic characteristics showed good agreement with the experimental results.

1. Introduction

One of the main concerns when designing long-span suspension bridges is the effects of aerodynamic forces, which can cause instability in the structure, including buffeting, fluttering, galloping, and vortex-induced vibrations (Miyata, 2003; LarsenGuy, 2015). These effects have been thoroughly investigated using approaches such as long-term on-site field measurements, wind-tunnel tests and numerical models to find the best management strategy.

From a practical point of view, wind tunnel tests on full size or scale bridge models offer a range of valuable outputs which can be effectively used when designing, constructing, and validating numerical models. However, wind tunnel tests do have several advantages, including scheduling availability, cost, short duration, and high reliability (Song et al., 2020). The main constraints on designing aeroelastic models are difficulties in constructing a real-size model and the small geometrical scale λ, which is limited by the wind tunnel dimensions (Argentini et al., 2016). Previous studies have suggested that a scaled-down model (1:200) of the complete structure and section models (1:25, 1:60, 1:80) tested in a wind tunnel overestimate the flow separation, and the Strouhal number and velocity obtained from the tests are both much lower than field measurements (Frandsen, 2001; Li et al., 2014).

The turbulence model based on the two-equation linear eddy-viscosity Reynolds Averaged Navier-Stokes simulation (RANS), Reynolds stress models (RSMs) or the large eddy simulation (LES), is receiving increasing attention as the CFD computational capability is developing. One of the most common turbulence models is the shear stress transport model (SST), which is a combination of the k-ε and k-ω turbulence models (where k, ε and ω are turbulent kinetic energy, dissipation rate and specific dissipation rate, respectively) and can perfectly predict the flow separation point (Škerlavaj et al., 2011).

The main objective of this work is to analyse the wind actions on a suspension pedestrian bridge located in Arouca, Portugal. At present, the 516 Arouca bridge is the longest suspension footbridge in the world

* Corresponding author. Itecons - Institute of Research and Technological Development in Construction, Energy, Environment and Sustainability, Rua Pedro Hispano, 3030-289, Coimbra, Portugal.
E-mail address: tadeu@itecons.uc.pt (A. Tadeu).

https://doi.org/10.1016/j.jweia.2021.104837
Received 25 March 2021; Received in revised form 11 October 2021; Accepted 11 November 2021
Available online 17 November 2021

with a span length of 516.5 m. The bridge is located in a mountainous area over the Paiva river at a height of 175 m. A three-dimensional CFD model of two attached half bridge decks exposed to wind with different angles of attack was analysed using ANSYS Fluent software (Fluent Versi, 2019). After confirming the mesh independence and the guarantee of free-field flow conditions, the CFD model is validated using results from experiments conducted on a scale model in a wind tunnel. The effects of wind angles of attack on the aerostatic stability of the bridge, considering the deck as a separate module, deck with guiding arch, and deck with guiding arch and secondary cables were comprehensively investigated. Although the Eurocode scope does not cover this type of bridge, given its span length, the results obtained when following its procedures are also compared with those given by the CFD model.

2. Analysed structure

The pedestrian suspension bridge is supported by two reinforced concrete pillars, 36.3 m tall, on the valley sides and attached to the ground. The bridge has a span of 516.5 m, suspended by means of a system of catenary cables and hangers (see Fig. 1). The distance between the main cables increases steadily from the middle of the bridge to the pillars. The deck board is suspended from the main cables by hangers (secondary cables).

The deck board consists of 127 metal modules, each being 4016 mm long and with a maximum width of 2100 mm. The ends of the modules are connected to the same node where the secondary cables are connected. The structure modules consist of UPN steel profiles (grade S275) and angle brackets. The connecting lugs to the hangers are at the outermost point of the frames, the connection is made by an M20 bolt and a single nut. The floor consists of metal rails 1.30 m wide, and the side guards, between the handrail and the floor, follow the shape of the frames with a grid. Both elements (floor and side guards) have high surface open grid areas (porosity >70%). The geometry of one module together with hangers is shown in Fig. 2.

3. Computational fluid dynamics analysis

In this study, ANSYS Workbench 2019 R3 software is used to solve the conservation equations for the entire solution domain using the finite volume method (Versteeg and Malalasekera, 2007a). The fundamental Navier-Stokes conservation equations of linear momentum and mass and state equations can be found in Cengel et al. (Cengel and Cimbala, 2006). The fluid flow is considered to be incompressible and in the turbulent regime at the inlet. The turbulent flow in this study was modelled using the Reynolds-Averaged Navier-Stokes equations and the k-ω SST model (Menter et al., 2003). The RANS equations are the most widely used class of turbulence models in applied research thanks to their fast computation time and excellent convergence characteristics (Durbin and Reif, 2011). The SST model has greatly benefited from the strength of the underlying turbulence model and covers a modified near-wall treatment of the equations to reduce the problem of grid-induced separation for industrial flow simulations.

The air flow was considered as steady-state and incompressible. A pressure-based solver was used, which requires less memory and allows flexibility in the solution procedure. The gradient of solution variables is required to evaluate diffusive fluxes and velocity derivative. The Green-Gauss-Cell-based approach was used for this purpose. The SIMPLEC algorithm (Versteeg and Malalasekera, 2007b) was used for the pressure-velocity coupling due to its robustness. The interpolation scheme for calculating cell-face pressure used the PRESTO! method, which is frequently used for flows involving steep pressure gradients or in strongly curved domains. The first-order upwind method was used for

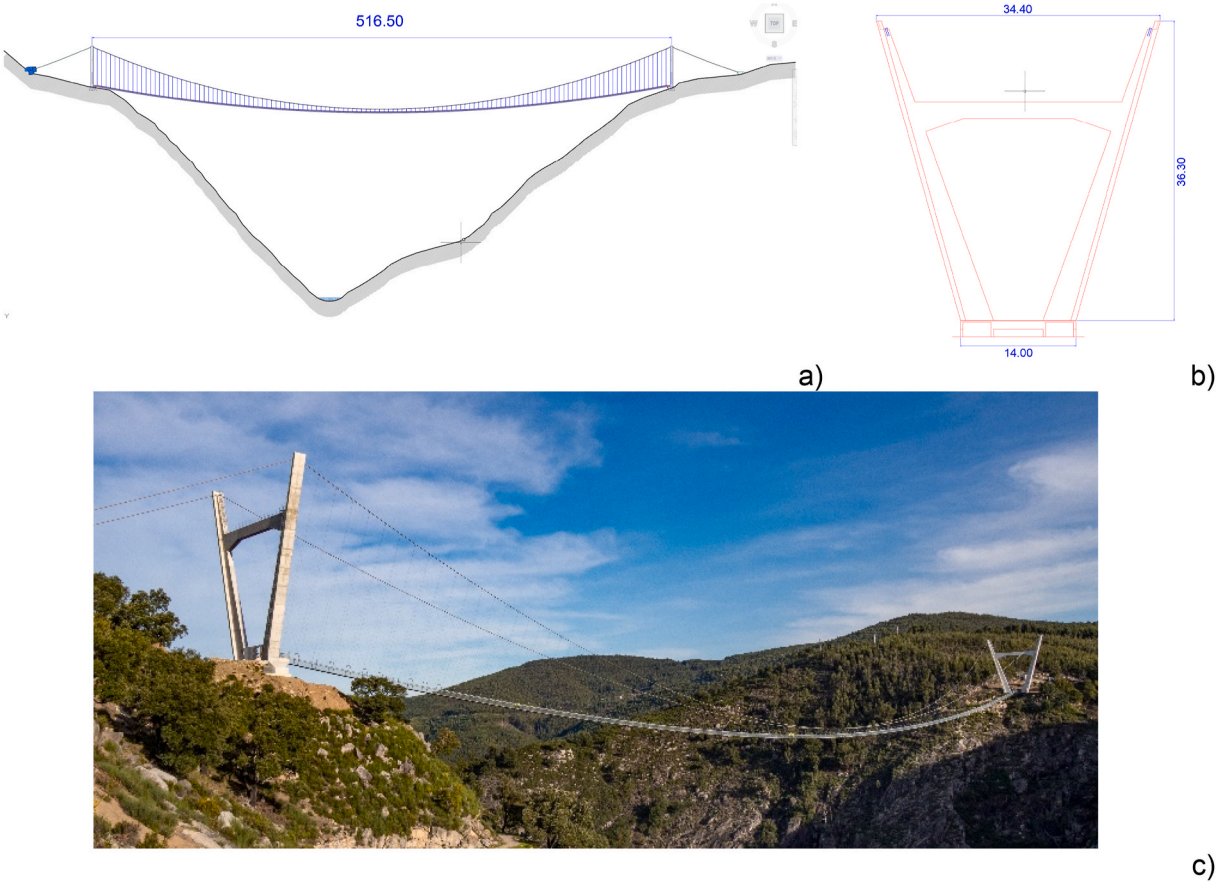

Fig. 1. 516 Arouca footbridge (Portugal): a) Longitudinal geometry (dimensions in meters); b) Pillars of the bridge (dimensions in meters); c) Actual view.

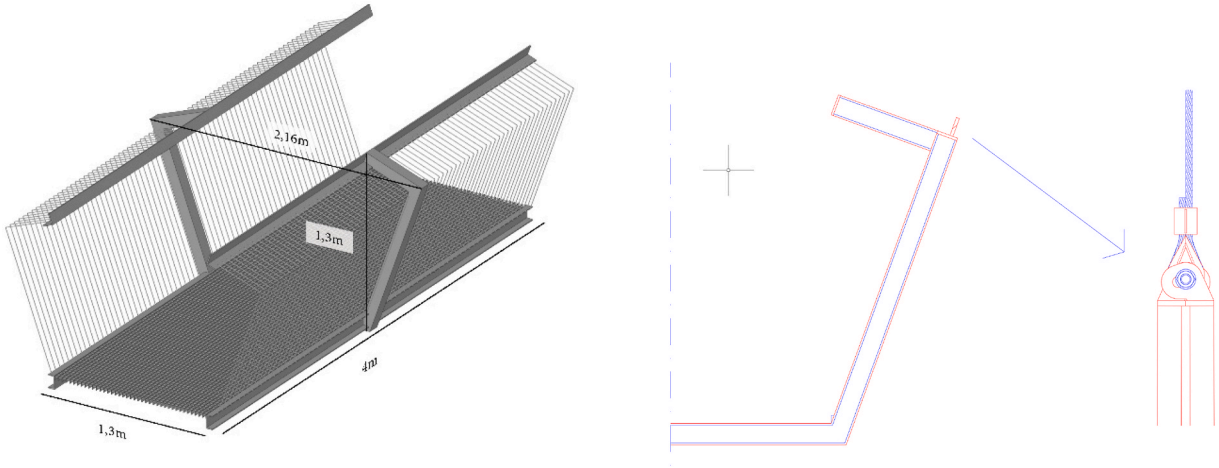

Fig. 2. The geometry of one module of the bridge and the hangers.

the remaining interpolation arrangements for robustness and easy convergence (Ferziger and Peric, 2002).

3.1. Computation of the aerodynamic coefficients

The aerodynamic coefficients, C_L, C_D and C_M, respectively lift, drag and moment (see Fig. 3), were evaluated by unit length for each tested angle of attack by the following equations:

$$C_L = \frac{L}{\frac{1}{2}\rho U^2 bl} \quad ; \quad C_D = \frac{D}{\frac{1}{2}\rho U^2 bl} \quad ; \quad C_M = \frac{M}{\frac{1}{2}\rho U^2 b^2 l} \tag{1}$$

where, ρ is the air density, U is the wind velocity, $b = 1.30$ m is the width of the deck and $l = 4.0$ m is the deck length; and L, D, M correspond to the lift, drag and moment forces (computed in relation to the centre of pressure, positioned at $d_{CG} = 0.628$ m from the deck floor).

3.2. Computational domain and mesh schemes

Two half deck modules, attached as in the real bridge, were modelled to represent the behaviour of the bridge. The size of the cross-section boundary was taken as 4.0×4.8 m^2, proportional to the wind tunnel dimension (used in the experimental tests). The module was modelled considering three different configurations of the bridge deck module (Fig. 4): a) module with handrails and guard; b) module with handrails, guard, and secondary cable guiding arch; c) module with handrails, guard, secondary cable guiding arch, and secondary cables. The module was also modelled for different wind angles of attack ranging from $-8^o \leq \alpha \leq +8^o$ to investigate the effect of descending and ascending wind. This was accomplished by rotating the model for different angles.

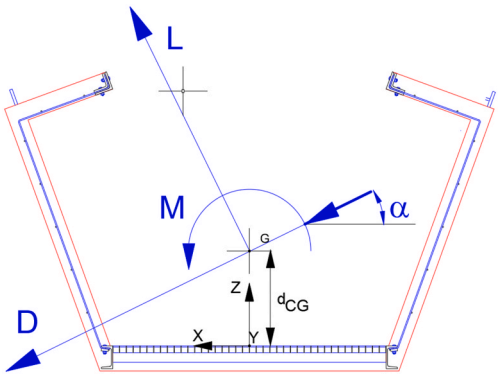

Fig. 3. Angle of wind attack.

The movement of the module is minimal, and it was not taken into account in this paper.

Three different boundary lengths were modelled to study the free stream condition, namely 12 m, 20 m, and 28 m, referred to in the rest of this paper as small, medium, and large, respectively. The upstream boundary size was kept constant in all models. Fig. 5 illustrates these models used for the CFD simulations. Constant inlet velocities and atmospheric pressure were imposed on the inlet and outlet boundary conditions, respectively. The boundary condition for the side walls was set as symmetry to assume the zero flux of all quantities across the boundary. This figure also illustrates the Cartesian coordinate system used.

Different meshes of the finite volume method were used to solve the governing fundamental equations of the fluid flow. This was achieved using ANSYS® Mesher (Fluent Versi, 2019). Non-structured tetrahedral meshes were defined. The meshes were then converted to polyhedral elements in Fluent software to increase precision, convergence, and robustness. Fig. 6 illustrates the type of mesh structure used in this model and the mesh refinement around the bridge floor and side guards with complex geometry. The meshes were optimized and partitioned in ANSYS Fluent using the Cuthill-McKee inverse method (Tu and Guan-HengLiu, 2012) and the METIS algorithm package for parallel computing (Karypis, 2011; Karypis and Kumar, 1998).

Coarse, medium and fine discretisation with different numbers of elements were used to ensure the accuracy of the solution and the grid independence (see Table 1).

The convergence of all variables, including the drag and lift coefficients, were checked for all the models. The input parameters for the CFD simulation were wind speed range 3.91–52.84 m/s, air density 1.225 kg/m^3 and air viscosity 1.7894e-05 kg/ms. In all models, the residuals were found to be very small and, as expected, they decrease as the number of iterations increases. The module with handrails, subjected to a horizontal wind ($\alpha = 0^o$) with speed set to 50 m/s, simulated with the medium model discretised with the medium discretisation, was selected to illustrate these results.

Fig. 7 shows the convergence of scaled residuals related to the mass and momentum equations, considering the continuity, the three velocity components, the turbulent kinetic energy k, and the specific dissipation rate ω.

The convergence analysis was also guaranteed by verifying representative velocities and pressure points around the bridge module. The receivers placed at points 1 (0.0, −2.0, 0.4) m, 2 (−0.9, −2.0, 0.5) m, 3 (0.9, −2.0, 0.5) m, 4 (−0.6, −2.0, 1.4) m and 5 (0.6, −2.0, 1.4) m in this same model (see Fig. 8) are used to illustrate the convergence of the model. Analysis of these figures allows the conclusion that the convergence is attained with very few iterations.

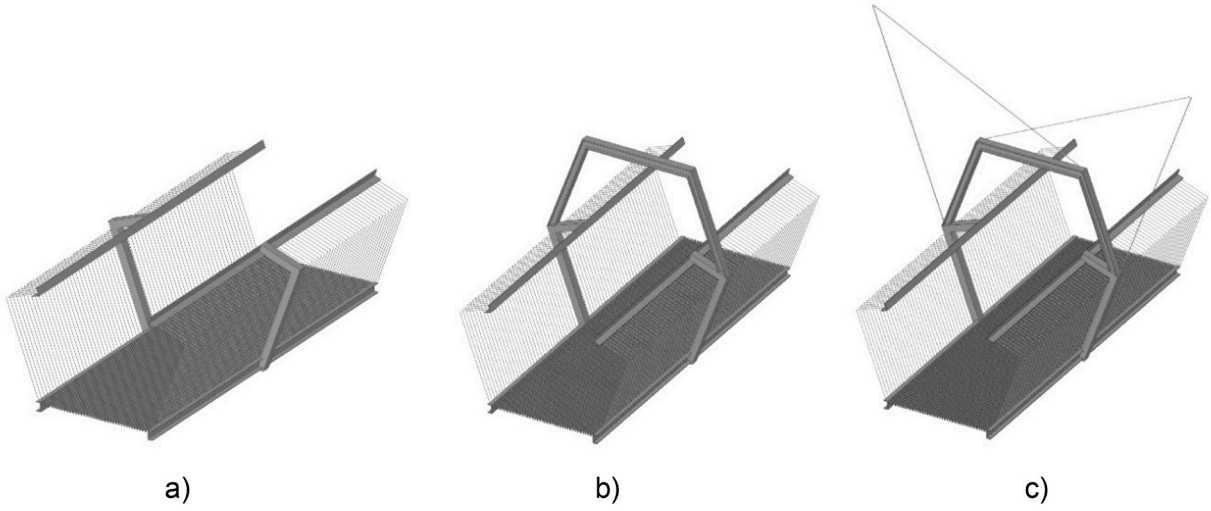

Fig. 4. Different geometries considered for modelling: a) module with handrails and guard; b) module with handrails, guard, and secondary cable guiding arch; c) module with handrails, guard, secondary cable guiding arch, and secondary cables.

The drag and lift coefficients were also monitored for all models to ensure convergence. The analysis of those results, presented in Fig. 9 for the same model, allows the conclusion that the drag coefficient converges for a low number of iterations. The lift coefficient, however, requires more iterations.

To ensure the accuracy of the solution and the grid independence, the drag and lift coefficients were computed for all models. Table 2 presents the results when the module with handrails is subjected to a horizontal wind of 50 m/s ($\alpha = 0^o$).

It can be seen that by increasing the domain size from 20 m to 28 m (medium to large), the associated drag and lift coefficients were almost unchanged. This behaviour is explained by the fact that the porosity of the bridge modules is very high, and increasing the downstream size from a certain level will not affect the free stream condition.

As shown in Table 3, for the small model, by increasing the number of elements from 7.5 to 12.3 million, the drag and lift coefficients changed by about 2.1% and 4.5%, respectively, while for the medium model the drag and lift coefficients changed by about 0.3% and 2.4%, respectively, when the number of elements was increased from 11 to 25 million. No changes were noted in the drag and lift coefficient values for the large model when the number of elements was increased from 16 to 47.5 million. Therefore, considering the higher computational cost for the large model and the small difference in the results, the medium grid size was selected for computations.

Table 3 includes the non-dimensional length scale y+ and the first layer thicknesses for different mesh structures. All y + values are below 1, meaning that a proper size of the cells near domain walls is used. These values become progressively smaller as the number of elements increases. This behaviour is also justified by creating the inflation layers around the bridge no-slip walls boundary with five layers and growth rate of 1.4 to ensure capture velocity gradient. The table shows the first layer's thickness imposed to obtain the desired y + value, while preserving the mesh quality.

3.3. Confirmation of the free flow conditions

The free flow conditions were demonstrated for all deck module configurations using the medium model with the medium discretisation. This was done by ascertaining the velocity field along different downstream cross sections and the longitudinal velocity streamlines. This analysis was complemented by detecting the existence of recirculation zones behind the bridge on the downstream side. In all cases, the imposed inlet wind velocity was 50 m/s.

To illustrate the results, Fig. 10 displays the velocity field along different downstream cross sections (x = 1.2 m, x = 6.0 m, x = 10.5 m and x = 14.0 m) for different wind angles of attack ($\alpha = -8^o$, $\alpha = 0^o$ and $\alpha = +8^o$) for two types of deck modules, namely with handrails and guard; with handrails, guard, and secondary cable guiding arch. In all cases, the larger oscillations in the wind velocity occur in the close vicinity of the bridge module, mainly around the junction section of the two module decks (y = − 2.0 m). The amplitude of these velocity oscillations becomes progressively smaller with the shift downstream, reaching at x = 14.0 m, a homogeneous wind velocity field of 50 m/s.

The longitudinal velocity streamlines, presented in Fig. 11a), confirm that free flow conditions have been attained. Horizontal streamlines can be observed as we move away from the bridge module to the downstream direction. It can also be seen that away from the junction section of its two module decks the wind can cross the bridge without significant perturbation. Directly behind this junction, the steel profiles create a shadow, preventing a considerable wind flow. This is clearer in the zoomed-in images presented in Fig. 11b), where it can also be seen that minimal recirculation zones appear behind the deck module. The longitudinal vector velocity field, illustrated in Fig. 12, shows that the recirculation zones are only generated in the close vicinity of the longitudinal deck and handrail steel profiles.

In general, the free flow boundary conditions should be specified at the distance downstream from the bridge where they do not affect the flow circumstances around the bridge. Since the floor and the side guards of the bridge have high surface open grid areas, therefore the bridge represents the high porosity solid structure with only minor effects on fluid flow circumstances. Since no extensive recirculation zones appear behind the bridge, both medium and large solution domain lengths are appropriate to prescribe the outflow boundary conditions for all solution cases.

4. Experimental tests

4.1. Test facility

The experimental tests were performed in a wind tunnel at the Centre of Seismic Engineering and Structural Dynamics (NESDE) of the Department of Structures (DE) of the National Civil Engineering Laboratory (LNEC).

The model scale λ = 1:4 was chosen to: i) have enough definition for the deck and handrail beam shapes; ii) avoid the effects associated with low Reynolds number; iii) reproduce a deck module (4 m), roughly 8%

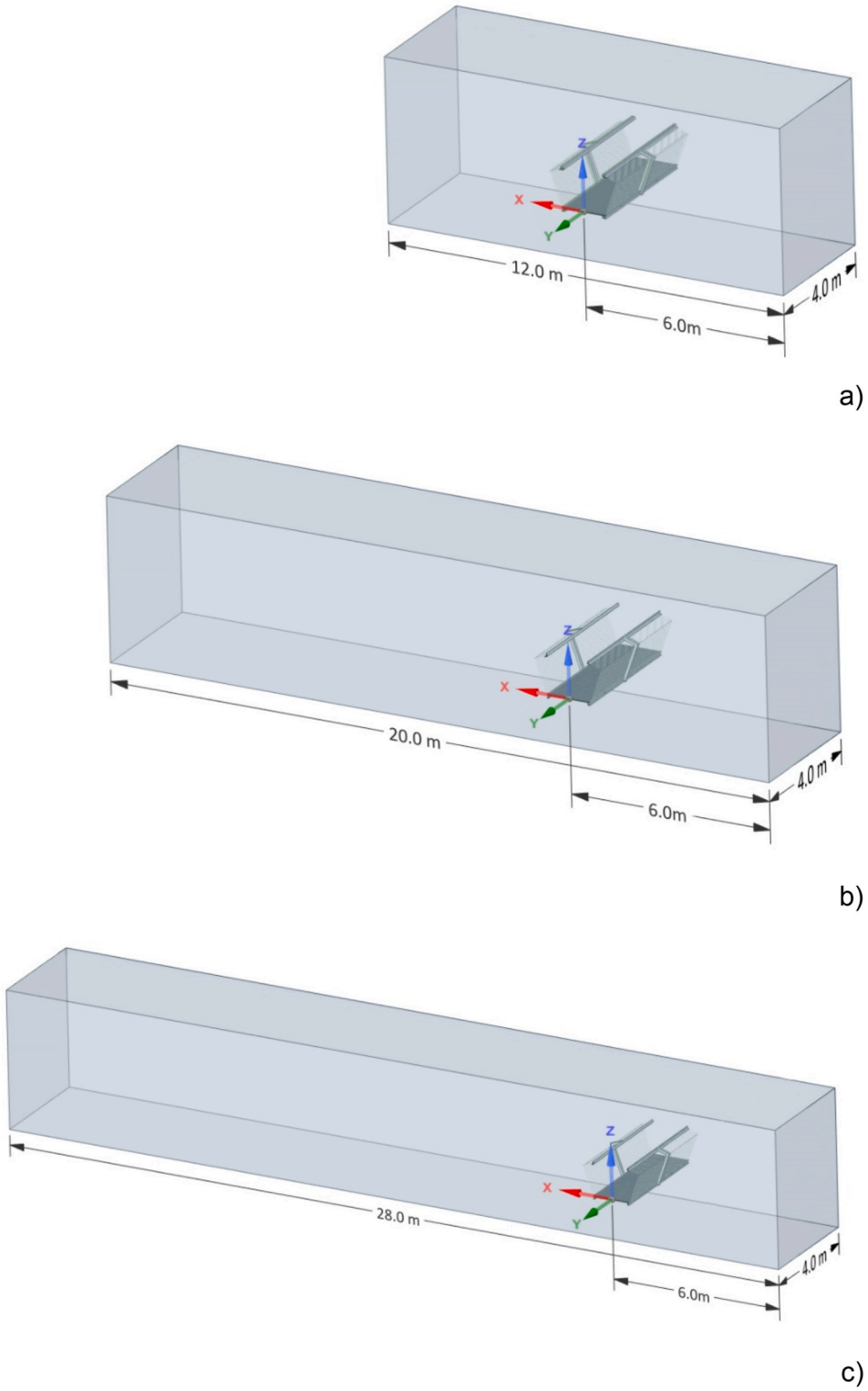

Fig. 5. The boundaries and fluid domain dimensions used for the CFD simulations: a) small model; b) medium model; c) large model.

of full length; iv) prevent blockage as, due to its large porosity (over 70% for deck and guard elements), it uses 4% of the wind tunnel cross section; and v) set Reynold number as $R_e = 5.0 \times 10^3$, from the smallest beam dimension, for the full range of test wind velocities.

The model reproduces two half deck modules with their U-shaped side and cross beams (steel) and floor mesh (PVC), guard mesh, double (face to face) U-shaped support beams (steel), L-shaped handrails (steel) and guard mesh (steel wire), as can be seen in Fig. 13. Both meshes reproduce the respective porosity. The total length is 1.0 m, and the deck is 0.325 m wide while the guard is 0.540 m wide and 0.325 m high.

Flat end plates were installed in order to keep a 2D flow around the model and prevent 3D effects around the model tops, rounded corners and thickness (Fig. 14). Sets of supporting external horizontal beams are connected to the end plates, allowing the model to be suspended inside the wind tunnel; the attachment point coincides with the centre of gravity.

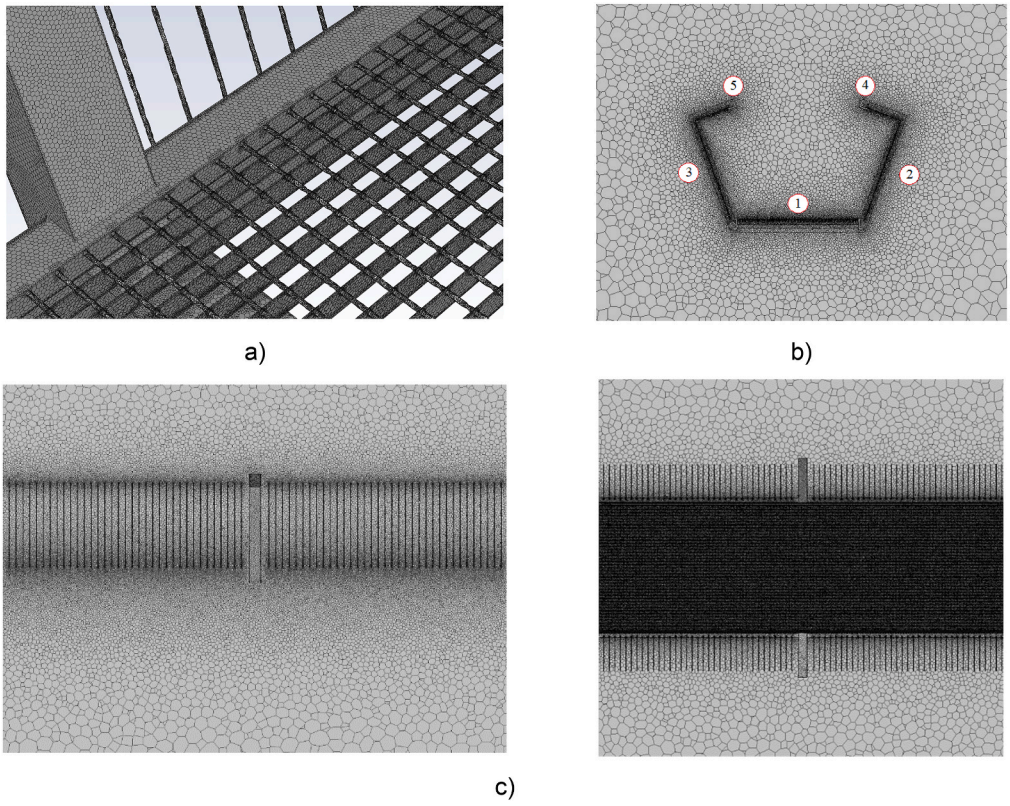

Fig. 6. Polyhedral mesh structure used in the medium model with medium discretisation: a) mesh refinement around the bridge floor and side guards; b) mesh refinement at y = −2 m and position of the receivers used to verify the convergence of the solution; c) mesh refinement at x = −1 m; d) mesh refinement around the floor at z = 0 m.

Table 1
The number of elements used to discretize the different models.

Discretisation	Small model	Medium model	Large model
Coarse	4 212 773	9 197 298	10 826 018
Medium	7 537 193	11 277 634	16 054 468
Fine	12 018 437	25 184 981	47 525 007

4.2. Wind tunnel and testing

The tests were performed in one of LNEC's wind tunnels (WT). It is an aeronautical type, closed-circuit WT with one fan controlled by a frequency variator that allowed the wind velocity to go up to about 45 m/s. The test chamber measures 1.0 × 1.2 × 3.0 m^3 (cross section of 1.20 m^2) and a uniform flow with low turbulence (<1%) [www.lnec.pt]. All tests were performed in an open test chamber.

The wind speed was evaluated from the flow dynamic pressure using a 5 mm Pitot-Prandtl tube connected to a Betz type precision micromanometer, through the following equation,

$$U = \sqrt{\frac{2q}{\rho}} \tag{2}$$

where U is the flow velocity [m/s] and q is the dynamic pressure [Pa].

The forces on the model were measured using six load cells Aihasd (5 kg max.), four for lift and two for drag, including previously calibrated full bridge strain gauges. Data were collected by an HBM *SPIDER* 8 unit.

4.3. Testing

The model is suspended by four sets of chain-spring-load cells (vertical forces – lift) connecting the horizontal beams to fixed points at WT roof level. A pair of external INVAR wires connect the suspension beams horizontally to fixed upwind points with interspersed load cells, thus preventing the downwind model displacement and measuring drag forces.

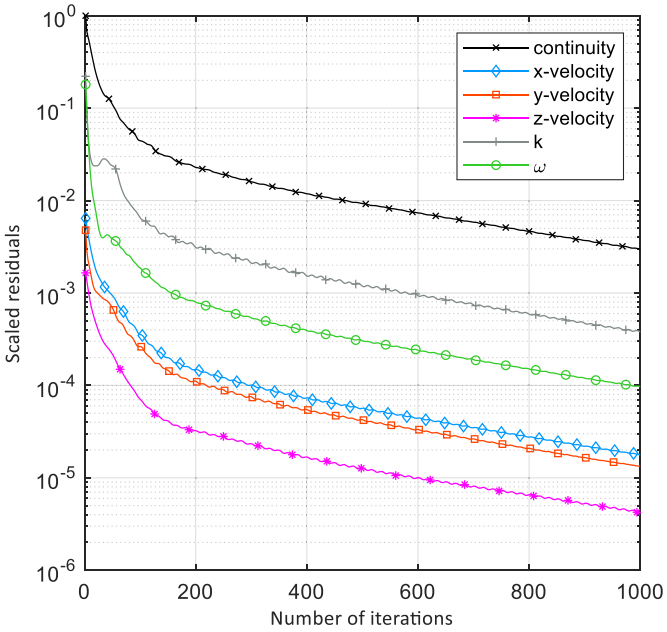

Fig. 7. Convergence of logarithmically scaled residuals registered for the medium model for the medium discretisation considering zero angle of attack $\alpha = 0^o$.

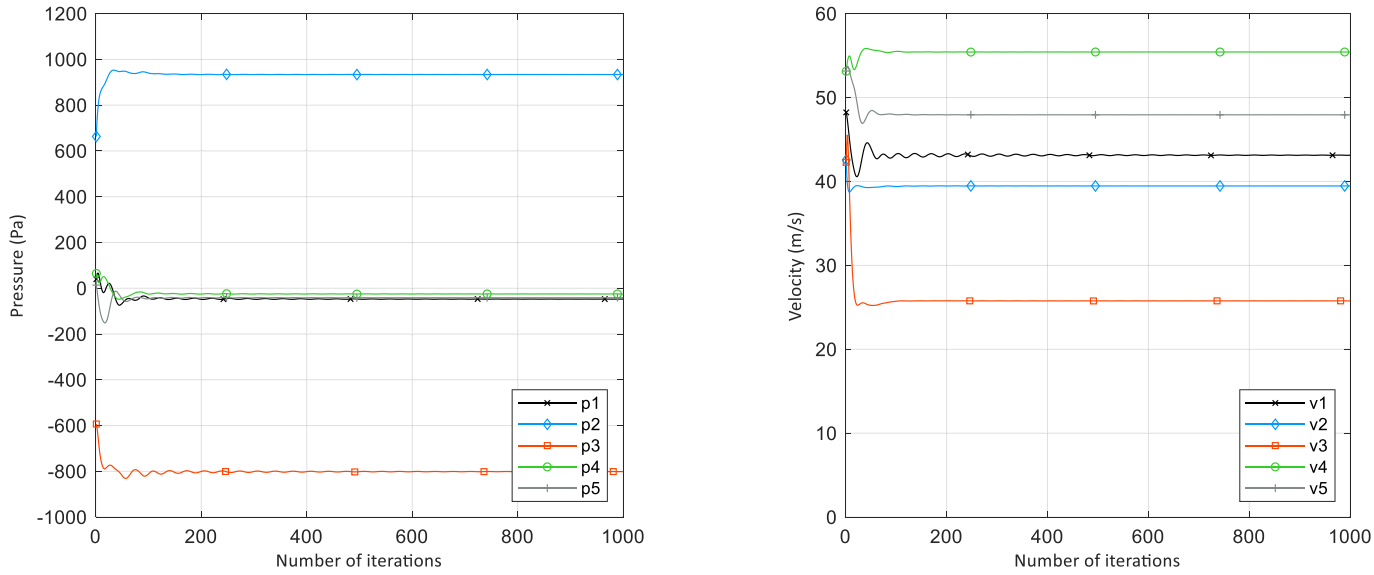

Fig. 8. Convergence of monitored variables (pressure and velocity) at receivers 1 to 5 registered for the medium model for the medium discretisation with zero angle of attack $\alpha = 0^o$.

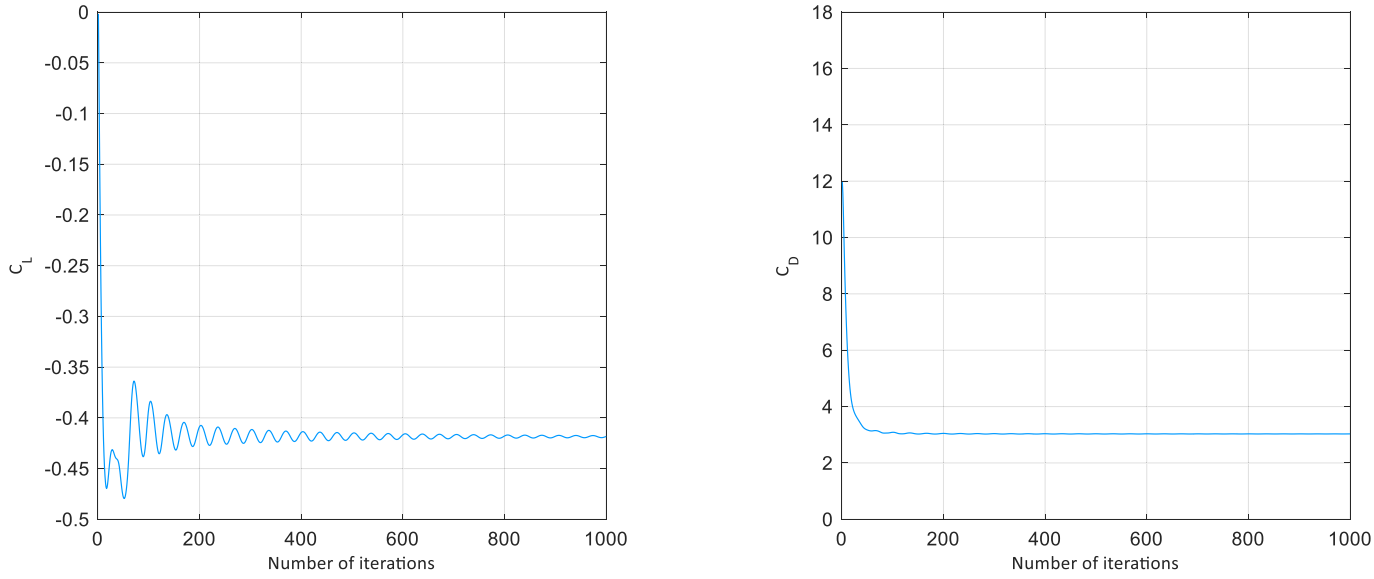

Fig. 9. Convergence of average lift (C_L) and drag (C_D) coefficients computed using the medium model results for the medium discretisation with zero angle of attack $\alpha = 0^o$.

Table 2
Grid independency analysis – C_D and C_L coefficients with zero angle of attack $\alpha = 0^o$.

Discretisation	Small model		Medium model		Large model	
	C_D	C_L	C_D	C_L	C_D	C_L
Coarse	3.41	−0.49	3.29	−0.48	3.28	−0.47
Medium	3.13	−0.41	3.02	−0.41	3.01	−0.40
Fine	3.07	−0.39	3.01	−0.40	3.01	−0.40

Table 3
Grid independency analysis for y+ and first layer thickness with zero angle of attack $\alpha = 0^o$.

Discretisation	Small model		Medium model		Large model	
	y+	th [mm]	y+	th [mm]	y+	th [mm]
Coarse	0.93	0.0139	0.81	0.0121	0.78	0.0121
Medium	0.53	0.0079	0.55	0.0079	0.53	0.0079
Fine	0.31	0.0042	0.28	0.0042	0.23	0.0042

The aerodynamic angle of attack was obtained by changing the length of the suspension chains (see Fig. 15). Positive values of α mean upward flow and vice-versa. The model is free to move vertically and in rotation, but not downwind. The lift forces are evaluated by adding the four vertical load cells' measurements, while the moments are computed by the difference between the upwind and downwind vertical load cells. Drag is evaluated by adding the two horizontal load cells' measurements. The aerodynamic forces and moments were then evaluated for a set of wind velocities up to 12 m/s. The data acquisition only started after stabilisation of the forces on the six load cells. The data are recorded for at least 60 s. The data are then analysed using the mean of the results obtained after the stabilisation of the forces on all load cells.

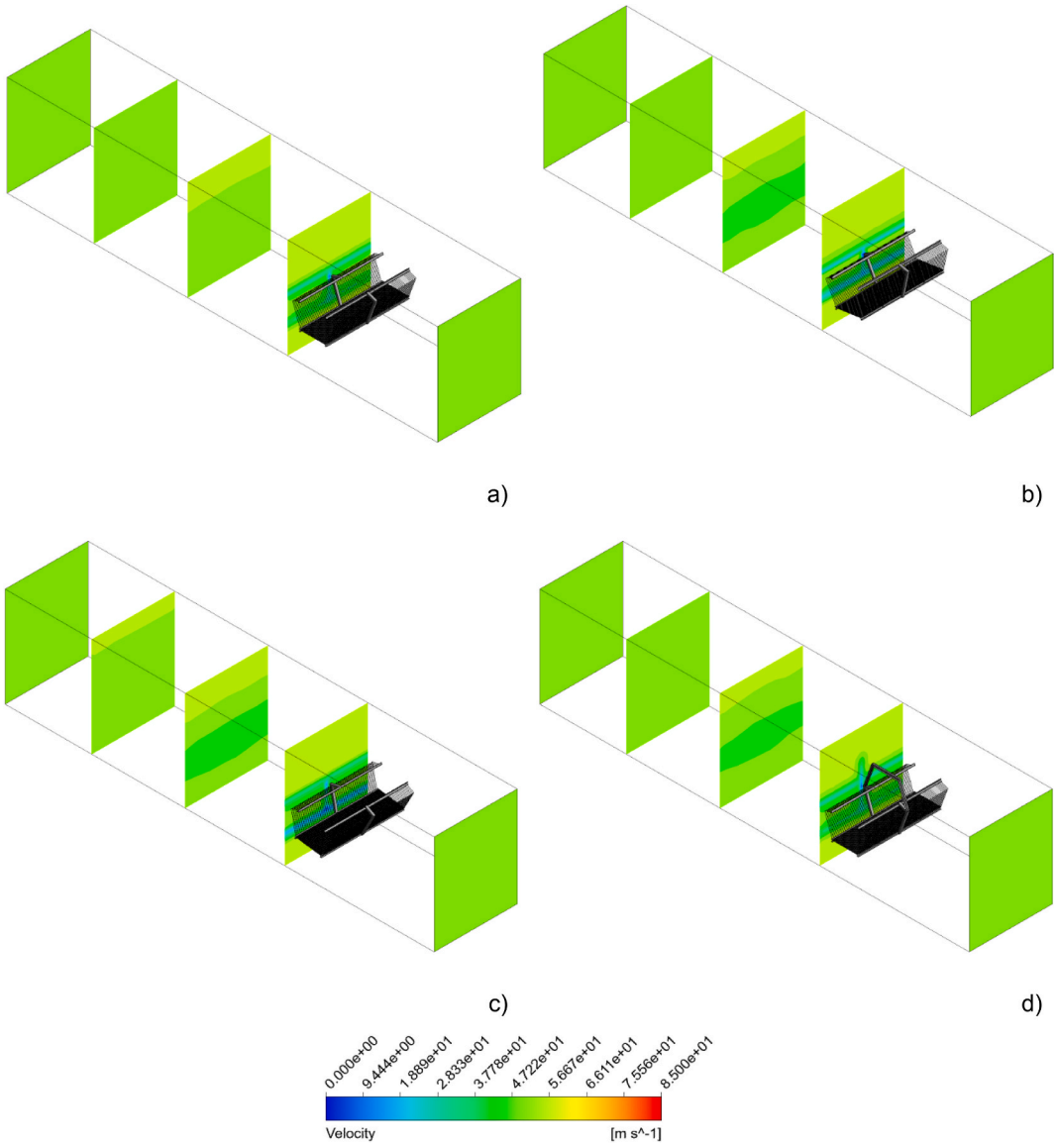

Fig. 10. Velocity field along different downstream cross sections (x = 1.2 m, x = 6.0 m, x = 10.5 m and x = 14.0 m) for different wind angles of attack: a) module with handrails and guard for $\alpha = 0^o$; b) module with handrails and guard for $\alpha = -8^o$; c) module with handrails and guard for $\alpha = +8^o$; d) module with handrails and guard and secondary cable guiding arch for $\alpha = 0^o$.

Linear regression is applied to the pairs of values F(U) – qA (see Fig. 16) for different wind angles of attack, where the dynamic pressure is obtained from Equation (2) and A is the reference area of the floor deck (0.325 m^2).

The respective aerodynamic coefficients, C_L, C_D and C_M were computed as in Eq. (1). The b and l assume, now, the following values $b = 0.325$ m is the width of the deck and $l = 1.0$ m. Fig. 16 illustrates the computation performed for $\alpha = 0^o$, $\alpha = -8^o$ and $\alpha = 8^o$. An excellent linear regression was found with a coefficient of determination close to 1 for all the computed angles of attack.

To evaluate the twisting on the reduced model the variation of the inclination of the deck module was measured using an inclination sensor from ASM (model PTAM27), using a frequency of acquisition of 10 Hz. Fig. 16 illustrates the results from the inclination sensor for angles of attack of -8°, 0°, +8° when in the presence of a wind with a velocity of U = 12 m/s (only the last 60 s). The results confirmed that the twisting of the model is so slight that it can be neglected. It was also noted that the vertical position of the deck does not change. These results are also consistent with the measured, small, moment forces, and with the linear regressions (with a coefficient of determination close to 1) found for the evaluation of the aerodynamic coefficients. This can be explained by the size of the openings of the surface grid areas of the bridge, which are quite large and thus create high porosity with little effect on the twisting of the bridge.

The tests were repeated for the bridge deck module and for the added upper arch and different angles of attack. For all cases, excellent linear regressions were found for the values of F(U) and qA. A similar behaviour was also found to that described before, that is, there was no twisting or vertical movement of the deck module.

5. Results and analysis

The experimental data obtained from the wind tunnel tests and the numerical results computed with the CFD model are presented in this subsection. The drag, lift and moment coefficients are compared for different wind attack angles. This analysis is carried out for three structure configurations: i) deck module, ii) deck module and arch, and iii) deck module, arch, and cables. Afterwards, this numerical model is

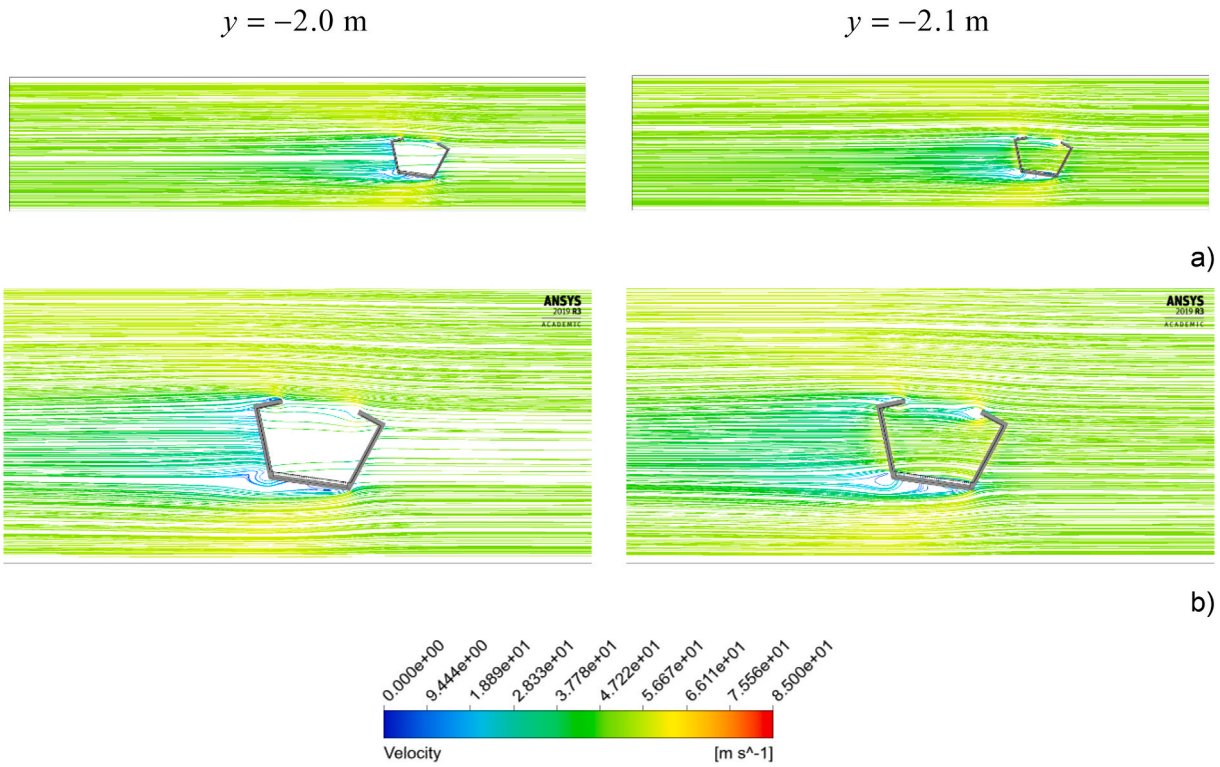

Fig. 11. Longitudinal velocity streamlines obtained when the module with handrails and guard is subject to a wind with an attack angle of $\alpha = +8^{o}$, at and $y = -2.1$ m and $y = -2.0$ m: a) full longitudinal field; b) detail of the longitudinal field in the vicinity of the deck module.

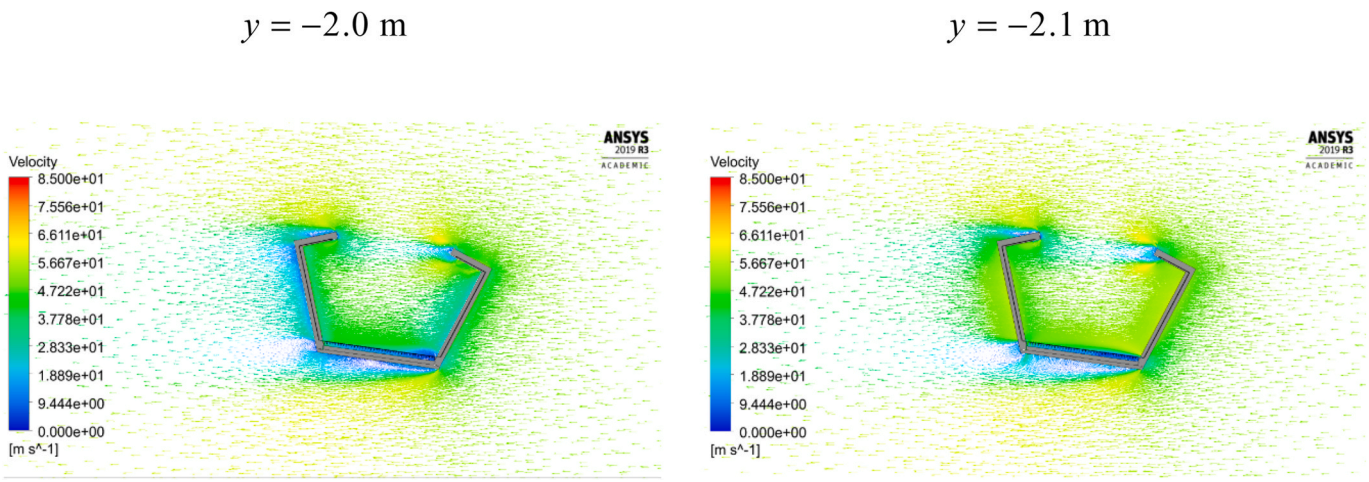

Fig. 12. Longitudinal vector velocity field obtained in the vicinity of the module with handrails and guard, subject to a wind with an attack angle of $\alpha = +8^{o}$, at $y = -2.1$ m and $y = -2.0$ m.

used to evaluate the contribution of the secondary cables to the dragging, lifting and moment forces. Thus, the results obtained using the Eurocode (NP EN 1991-1-4:2010) (European Committee for St, 2010) procedures are compared with those computed with the CFD model.

The bridge modelling took into consideration the bridge deck module, the bridge deck module with handrails and guard, adding the secondary cable guiding arch, and adding the secondary cables (not tested experimentally). The resulting drag and lift coefficients are listed in Table 4. The experimental results obtained described above are also included. The analysis of these results shows that the numerical results are similar to those recorded experimentally (when $\alpha = 0^{o}$).

Similar drag and lift coefficients were numerically found for lower velocities under steady-state conditions.

The drag, lift and moment coefficients were also obtained from CFD simulations for different angles of wind attack that represent the ascending and descending wind directions (from -8° to +8°) and these were compared with the results from wind tunnel tests.

As shown in Fig. 17, the drag coefficients computed by the CFD model for the bridge deck are similar to those obtained experimentally (maximum difference of 0.08). The drag coefficients computed by the CFD model tend to increase as the angle of the wind changes from the horizontal direction for both directions. When the arch is included, the experimental drag coefficients are slightly higher than those obtained numerically. For the drag coefficients obtained numerically, the smallest value is again found for the horizontal direction. Similar values are obtained for the case that includes the secondary cables.

Fig. 13. The model's deck beam, floor mesh and guard mesh.

Fig. 14. The model installed in the wind tunnel.

Fig. 15. Setting the angle of attacks using the suspension chains.

As expected, the lift coefficients are much smaller than the drag coefficients. The numerical results show a slight decrease as the wind angle of attack varies from -8° to +8°. Although exhibiting some fluctuations as the angle of attack changes, the experimental results show a similar tendency. The lift coefficients computed numerically for the cases that include the arch and secondary cables are similar to those calculated only with the bridge deck.

The numerical results for the moment coefficients only for the deck are almost null for the various wind angles of attack. The moment coefficients obtained experimentally show some variations, particularly when the wind angle of attack becomes positive. The maximum moment coefficient was recorded for $\alpha = -8^{o}$ (0.06). The presence of the arch leads to slight variations for both numerical and experimental approaches.

The drag forces obtained for different velocities from the CFD model are also compared with those following the recommendation given in Eurocode (NP EN 1991-1-4:2010) (European Committee for St, 2010), which would apply to the bridges with a span length up to 200 m (if the dynamic response is considered). The equivalent wind velocity, v_p, was obtained by assuming a ground of terrain category II, a basic wind velocity, v_b, up to $v_{b,0} = 27.0$ m/s (according to the Portuguese National Annex of NP EN 1991-1-4:2010).

The wind action for the bridge was then evaluated as the total sum over the individual structural elements of the bridge (cables and deck elements), based on the geometric characteristics of each component,

$$F_D = c_s c_d \sum_{elements} c_f q_p(z) A_{ref} \tag{3}$$

where $c_s c_d$ is the structural factor, c_f the force coefficient, $q_p(z) =$

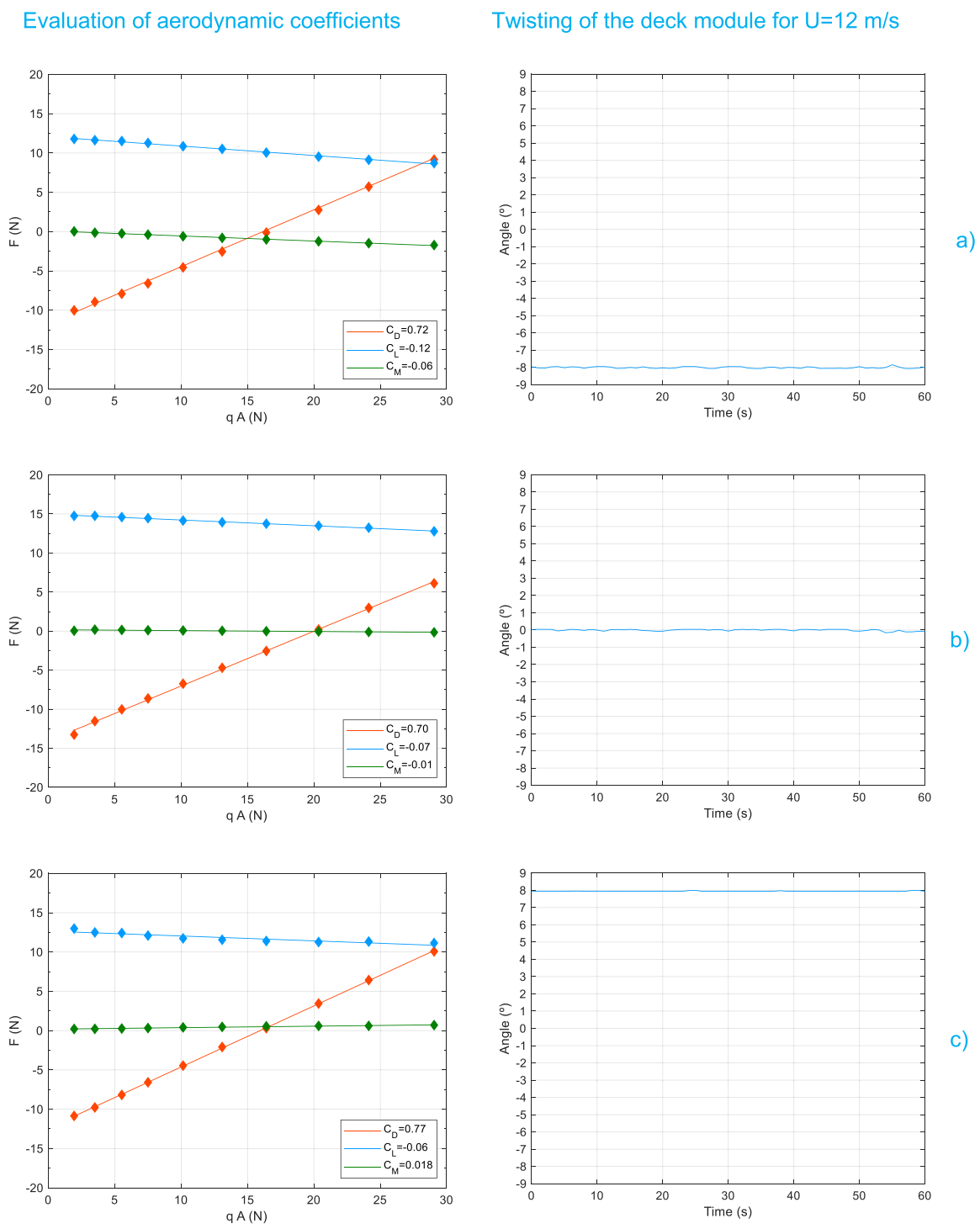

Fig. 16. Evaluation of aerodynamic coefficients and twisting of the deck module for different angles of attack: a) $\alpha = -8^o$; b) $\alpha = 0^o$; c) $\alpha = 8^o$.

$\frac{1}{2}\rho[v_p(z)]^2$ is the dynamic (velocity) pressure and A_{ref} is the reference area of the structure of the structural element.

The structural factor and the force coefficient were calculated according to the procedure included in NP EN 1991-1-4: 2010, which depends on the wind turbulence and the structure's natural frequency (0.116 Hz).

Table 5 shows the comparison between the horizontal force obtained from CFD results (for $\alpha = 0^o$) and the results following the procedure described above. The two results show excellent agreement, and thus the recommendations given by the NP EN 1991-1-4: 2010 are still applicable to this pedestrian suspension bridge.

6. Conclusions

An experimental and numerical study was carried out on the aerodynamic performance of a long-span suspension bridge, the 516 Arouca bridge, in a hilly location in Portugal. The RANS method proved to be a useful approach to model the fluid flow around the bridge. The numerical results were validated by experimental wind tunnel test results.

The analysis of the numerical results for the different downstream

Table 4
CFD and wind tunnel test results for different geometries considered; values are at zero angle of attack $\alpha = 0^o$.

Bridge module	CFD		Wind tunnel test		Absolute Error	
	C_D	C_L	C_D	C_L	C_D	C_L
Deck module	0.70	−0.09	0.70	−0.07	0.00	0.02
Deck module + arch	0.75	−0.11	0.83	−0.05	0.08	0.06
Deck module + arch + Cables	0.76	−0.12	–	–	–	–

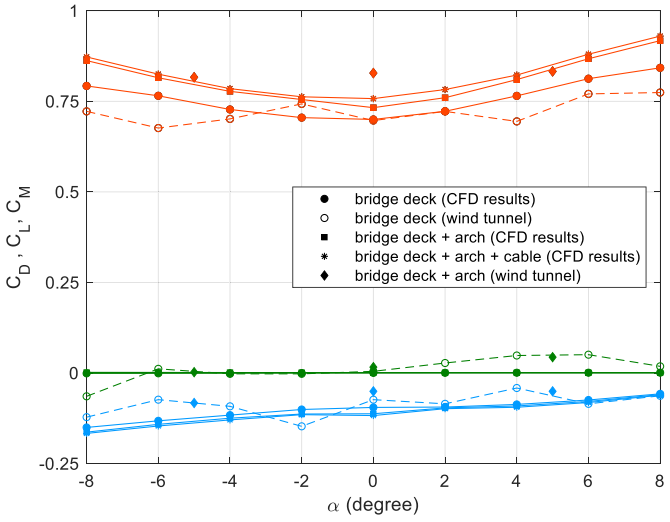

Fig. 17. Drag (red lines), lift (blue lines), and moment (green lines) coefficients: wind tunnel test results versus numerical results. (For interpretation of the references to colour in this figure legend, the reader is referred to the Web version of this article.)

Table 5
Total horizontal force (*FD* [KN/m]) under the wind action for different wind velocities and at zero angle of attack ($\alpha = 0^o$), Eurocode and CFD results.

$v_p(z)$ [m/s]	Deck Module		Deck module + arch	
	Eurocode	CFD	Eurocode	CFD
52.84	1.560	1.611	1.947	1.994
43.05	1.039	1.070	1.297	1.324
33.27	0.623	0.639	0.778	0.791
23.48	0.312	0.318	0.390	0.394
13.7	0.107	0.108	0.134	0.134
3.91	0.009	0.009	0.011	0.011

sizes showed that the high opening surface grid areas of the bridge create high porosity with little effect on the downstream wind flow. This result was influential in selecting the appropriate fluid domain size in which both the free flow condition and computation time were satisfied.

The results also showed that changes in the wind attack angles introduce some variations in the lift and drag coefficients. Adding the upper arch and secondary cables to the bridge deck slightly increases the drag coefficients. The drag coefficients computed by the CFD model for the bridge deck are similar to those obtained experimentally (maximum difference of 0.09). The lift coefficients were found to be much smaller than the drag coefficients, which was expected. The numerical results show a slight decrease as the wind angle of attack varies from -8° to +8°. Although exhibiting some fluctuations as the angle of attack changes, the experimental results show a similar tendency.

The agreement between the resulting CFD computed forces under the wind action for different inlet velocities and those provided by Eurocode calculations was quite good. Amplitude force differences of −1.9%–3.3% for the deck module and a force difference of −0.7%–2.4% for the deck with the upper arch were found for the velocities equal to 3.91 m/s and 52.84 m/s, respectively.

CRediT authorship contribution statement

António Tadeu: Conceptualization, Methodology, Supervision, Writing – review & editing, Formal analysis. **F. Marques da Silva:** Validation, Writing – review & editing, Formal analysis. **Bahareh Ramezani:** Methodology, Software, Writing – review & editing. **António Romero:** Conceptualization. **Leopold Škerget:** Methodology, Writing – review & editing, Formal analysis. **Filipe Bandeira:** Formal analysis.

Declaration of competing interest

The authors declare that they have no known competing financial interests or personal relationships that could have appeared to influence the work reported in this paper.

Acknowledgements

The authors would like to acknowledge the support provided by Arouca Town Hall (Câmara Municipal de Arouca), with special thanks to the President, Margarida Belém, and the Council Engineer, Conceição Oliveira. The authors are also grateful for the Portuguese Pluriannual Base Funding for Interface Centres (CIT/2018/23), supported by the FITEC – "Fundo de Inovação, Tecnologia e Economia Circular". Finally, the authors would also like to acknowledge the financial support provided by the Spanish Ministry of Science, Innovation and Universities (PID 2019-109622RB), and by the FEDER Andalucía 2014–2020 Operational Programme (US-126491).

References

Argentini, T., Diana, G., Rocchi, D., Somaschini, C., 2016. A case-study of double multimodal bridge flutter: experimental result and numerical analysis. J. Wind Eng. Ind. Aerod. 151, 25–36.
Cengel, Yunus A., Cimbala, John M., 2006. Fluid Mechanics-Fundamentals and Applications. McGraw-Hill.
Durbin, P.A., Reif, B.A., 2011. Statistical Theory and Modeling for Turbulent Flow. John Wiley & Sons, Ltd, New York.
European Committee for Standardization, 2010. Eurocode 1: Actions on Structures - Part 1-4. General actions - Wind actions.
Ferziger, J.H., Peric, M., 2002. Computational Methods for Fluid Dynamics. Springer Science & Business Media.
ANSYS, 2019. ANSYS Fluent Version 2019 R3.
Frandsen, J.B., 2001. Simultaneous pressures and accelerations measured full-scale on the Great Belt East suspension bridge. J. Wind Eng. Ind. Aerod. 89, 95–129.
Karypis, G., 2011. *METIS and ParMETIS*, Encyclopedia of Parallel Computing. Springer, pp. 1117–1124.
Karypis, G., Kumar, V., 1998. A Software Package for Partitioning Unstructured Graphs, Partitioning Meshes, and Computing Fill-Reducing Ordering of Sparse Matrices. University of Minnesota, Department of Computer Science Engineering Army HPC Research Centre, Minneapolis.
Larsen, Allan, Guy, L., 2015. Larose: *Dynamic wind effects on suspension and cable-stayed bridges*. J. Sound Vib. 334, 2–28.
Li, Hui, Laima, Shujin, Zhang, Qiangqiang, Li, Na, Liu, Zhiqiang, 2014. Field monitoring and validation of vortex-induced vibrations of a long-span suspension bridge. J. Wind Eng. Ind. Aerod. 124, 54–67.
Menter, F.R., Kuntz, M., Langtry, R., 2003. Ten years of industrial experience with the SST turbulence model. Turbul. Heat Mass Transf. 4. Begell House.
Miyata, Toshio, 2003. Historical view of long-span bridge aerodynamics. J. Wind Eng. Ind. Aerod. 91, 1393–1410.
Škerlavaj, A., Škerget, L., Ravnik, J., Lipej, A., 2011. Choice of a turbulence model for pump intakes. J. Power Energy 225 (6), 764–778.
Song, Jia-Ling, Li, Jia-Wu, Flay, Richard G.J., 2020. Field measurements and wind tunnel investigation of wind characteristics at a bridge site in a Y-shaped valley. J. Wind Eng. Ind. Aerod. 202, 104199.

Tu, Jiyuan, Guan-Heng, Yeoh, Liu, Chaoqun, 2012. Computational Fluid Dynamics: a Practical Approach. Butterworth-Heinemann.
Versteeg, H.K., Malalasekera, W., 2007a. An Introduction to Computational Fluid Dynamics: the Finite Volume Method. Pearson Education.
Versteeg, H.K., Malalasekera, W., 2007b. An Introduction to Computational Fluid Dynamics. Pearson, Glasgow.